DAVIS: A direct algorithm for velocity-map imaging system

G. R. Harrison, J. C. Vaughan, B. Hidle, and G. M. Laurent

Articles you may be interested in

Perspective: Advanced particle imaging
The Journal of Chemical Physics **147**, 013601 (2017); 10.1063/1.4983623

Excited state non-adiabatic dynamics of the smallest polyene, trans 1,3-butadiene. I. Time-resolved photoelectron-photoion coincidence spectroscopy
The Journal of Chemical Physics **148**, 164302 (2018); 10.1063/1.5016452

A multi-plate velocity-map imaging design for high-resolution photoelectron spectroscopy
The Journal of Chemical Physics **147**, 094201 (2017); 10.1063/1.4996011

Excited state non-adiabatic dynamics of the smallest polyene, trans 1,3-butadiene. II. Ab initio multiple spawning simulations
The Journal of Chemical Physics **148**, 164303 (2018); 10.1063/1.5018130

Velocity map imaging of ions and electrons using electrostatic lenses: Application in photoelectron and photofragment ion imaging of molecular oxygen
Review of Scientific Instruments **68**, 3477 (1997); 10.1063/1.1148310

Time-resolved photoelectron spectroscopy of adenosine and adenosine monophosphate photodeactivation dynamics in water microjets
The Journal of Chemical Physics **148**, 194303 (2018); 10.1063/1.5027258

DAVIS: A direct algorithm for velocity-map imaging system

G. R. Harrison, J. C. Vaughan, B. Hidle, and G. M. Laurent[a)]
Physics Department, Auburn University, Auburn, Alabama 36849, USA

In this work, we report a direct (non-iterative) algorithm to reconstruct the three-dimensional (3D) momentum-space picture of any charged particles collected with a velocity-map imaging system from the two-dimensional (2D) projected image captured by a position-sensitive detector. The method consists of fitting the measured image with the 2D projection of a model 3D velocity distribution defined by the physics of the light-matter interaction. The meaningful angle-correlated information is first extracted from the raw data by expanding the image with a complete set of Legendre polynomials. Both the particle's angular and energy distributions are then directly retrieved from the expansion coefficients. The algorithm is simple, easy to implement, fast, and explicitly takes into account the pixelization effect in the measurement. *Published by AIP Publishing.*
https://doi.org/10.1063/1.5025057

I. INTRODUCTION

Among the various techniques available to study the physics of the light-matter interaction, Velocity Map Imaging (VMI) systems emerged as a *first-choice* option as they simultaneously give access to the angular and energy distributions of the particles (electrons or ions) emerging from an interaction while retaining a high angular and energy resolution.[1,2] In addition, they also offer a 4π collection angle and a very high count rate, which is adequate for many experiments performed with relatively unstable light sources like laser systems. On the basis of all these assets, VMI systems have been extensively employed over the last three decades to study fundamental aspects of a variety of physical and chemical phenomena like photoionization, photodetachment, and molecular photofragmentation dynamics.[3]

The technique consists of projecting the particles emerging from the light-target interaction onto a planar position sensitive detector by means of an electrostatic lens, as shown in Fig. 1. As they travel toward the detector, the particles expand on the surface of a sphere (generally called a "Newton" sphere) whose increasing radius r is proportional to the product of their initial velocity v and their time of flight. The two-dimensional (2D) image $P(x, z)$ formed by their impact positions on the detector is then directly related to the initial three-dimensional (3D) distribution $I(r(v), \theta, \varphi)$ of the emission by the well-known Abel transform,[4]

$$P(x, z) = 2 \int_R^\infty \frac{I(r(v), \theta, \varphi) r}{\sqrt{r^2 - R^2}} \, dr, \tag{1}$$

where $R = \sqrt{x^2 + z^2}$ is the radial position of a given point in the projection and θ and φ are the polar and azimuthal emission angles of the particles, respectively. From a purely mathematical point of view, the exact three-dimensional distribution $I(r, \theta, \varphi)$ can be retrieved from the 2D projection

$P(x, z)$ through application of the inverse Abel transform,[4] provided that the emission possesses a cylindrical symmetry about an axis parallel to the plane of the detector, which is generally the case when linearly polarized light and randomly oriented targets are used in the experiment. However, because the Abel inversion is highly sensitive to any noise, fluctuations, or sharp features in the input data, this approach turns out to be non-practical when applied to a set of experimental data as it often leads to a solution very different from the true one.[5]

The literature is rich with studies reporting sophisticated methods and strategies to circumvent the inverse Abel transform. One elegant approach consists of imaging only a slice of the 3D velocity image, which contains all the information regarding the initial energy and angular distributions of the physical system.[6–11] Nevertheless, such an approach is generally not suitable for low mass particles that have a short time of flight such as protons or photoelectrons, as the response time of the detection system is often too slow to ensure the proper timing for the measurement. As a result, methods based on an analytical or numerical analysis of the projection of the full 3D distribution onto the detector are still very popular in the VMI's user community. A non-exhaustive list of widely used techniques includes the Fourier-Hankel method,[12,13] which is known to be computationally fast but also leads to an accumulation of noise along the centerline of the resulting 3D image, the onion-peeling technique[14–20] which is simple to implement and can be used (under certain conditions) in cases where the particle's emission does not possess a cylindrical symmetry,[21] and the forward convolution procedures such as the iterative algorithm[22] or the polar basis-set expansion (p-BASEX) method[23,24] which are particularly successful in handling low-quality images and produce smooth reconstructed pictures where the noise accumulates at the center spot. Despite the wealth of techniques available, the inversion problem remains an ongoing subject of study[25–31] as algorithms with improved accuracy, speed, and versatility are still highly desirable.

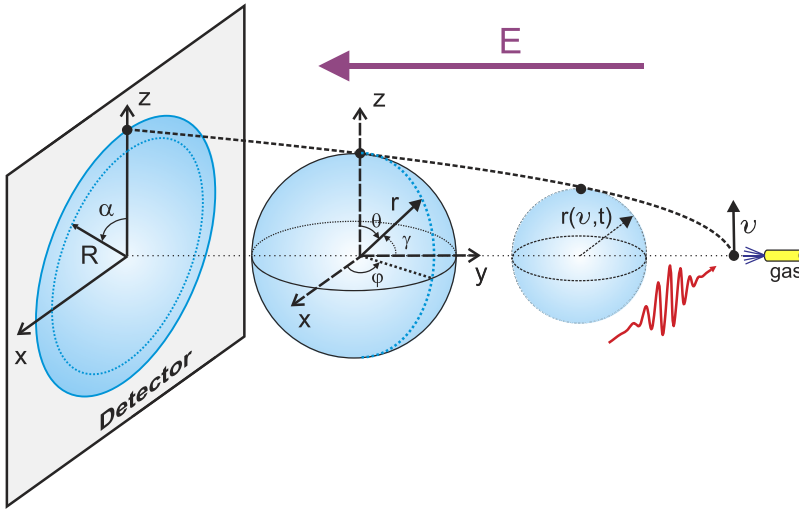a)Electronic mail: glaurent@auburn.edu

FIG. 1. Schematic of the velocity map imaging technique. Photoions or photoelectrons emerging from the interaction between a gas target and electromagnetic radiation are extracted toward a position sensitive detector by means of an electrostatic lens.

In this article, we present a direct (non-iterative) algorithm to retrieve the full three-dimensional velocity distribution of the emerging particles from its projected 2D image that bears a similarity to the pBASEX method.[24] Like pBASEX, our method consists of fitting the experimental data with the two-dimensional projection of a model 3D velocity distribution defined by the physics of the light-matter interaction.[32,33] However, while pBASEX uses a projection function resulting from a numerical integration of Eq. (1), our method is based on a proper analytical representation of the projection, which is expanded as a sum of Legendre polynomials. Both the velocity and velocity-dependent angular distributions are then directly retrieved from the resulting expansion coefficients by using an analytical inversion procedure. Our method offers two main advantages over pBASEX. First, it is less sensitive to noise and/or background as the meaningful angle-correlated information is extracted from the raw data by the Legendre polynomial expansion before inversion. Second, it is computationally much cheaper as the two-dimensional projection function is evaluated analytically rather than numerically and because the inversion procedure involves matrices of lower dimension compared to those embedded in pBASEX. Overall, our algorithm is simple, easy to implement, and allows on-the-fly inversion of measured images, which is well-suited for experiments that require fast image-based feedback such as coherent-control[20] or pump-probe[34–37] experiments. The method is described here for the particular case of photoionization with linearly polarized light, but it can be readily extended to the case of photoionization with circularly or unpolarized light.

II. METHOD

A. The measured two-dimensional image

In a general photoionization experiment with linearly polarized incoming light and randomly oriented targets, the three-dimensional velocity-space distribution $I(\boldsymbol{v})$ of any emerging particles (electrons and ions) possesses a cylindrical symmetry about the polarization's direction (i.e., there is no dependence on the azimuthal angle φ). In addition,

it can be written as the product of the particle's velocity distribution $F(v)$ and its velocity-dependent angular distribution $G(v, \theta)$,

$$I(\boldsymbol{v}) = I(v_x, v_y, v_z) = I(v, \theta) = F(v)G(v, \theta), \quad (2)$$

where v and (v_x, v_y, v_z) are the magnitude and components of the particle's velocity $\boldsymbol{v}$, respectively, and θ is the particle's angle of emission with respect to the polarization direction, as defined in Fig. 1. By expressing the velocity-dependent angular distribution $G(v, \theta)$ as a sum of Legendre polynomials,[32,33] Eq. (2) becomes

$$I(v, \theta) = F(v) \sum_{n=0}^{2N} \beta_n(v) P_n(\cos \theta), \quad (3)$$

where β_n is the asymmetry parameter associated with the Legendre polynomial $P_n(\cos \theta)$ of order n (with $\beta_0 = 1$) and N is the total number of photons absorbed by the target.

As the particles travel toward the detector, they expand on the surface of the "Newton" sphere whose radius r is proportional to the magnitude of their initial velocity v. At the detector, the analytical representation of the 2D image formed by their impact position is obtained by combining Eqs. (1) and (3),

$$S(R, \alpha) = \sum_{n=0}^{2N} 2 \int_R^{\infty} \frac{F(r)\beta_n(r)r}{\sqrt{r^2 - R^2}} P_n(\cos \theta) \, dr, \quad (4)$$

where (R, α) are the polar coordinates of a given point in the 2D image as defined in Fig. 1. By recognizing that $\cos \theta = R/r \cos \alpha$ and expressing $P_n(\cos \theta)$ as a function of $P_k(\cos \alpha)$,[38] Eq. (4) can be rewritten as

$$S(R, \alpha) = \sum_{n=0}^{2N} \sum_{k=0}^{\lfloor n/2 \rfloor} \sum_{l=0}^{\max\{k-1,0\}} C_{nkl} \int_R^{\infty} F(r)\beta_n(r)$$
$$\times \gamma_{nkl}(r, R) \, dr P_{n-2k}(\cos \alpha), \quad (5)$$

where

$$C_{nkl} = \frac{(-1)^{k-l} 2^{2l+1}}{(k-l)!} c_{nkl} \quad (6)$$

with

$$c_{nkl} = \frac{(n-k+l-1/2)^{\underline{k-l}}(n-k)^l(n-2k+2l-1/2)^{\underline{2l}}}{(2l)^{\underline{2l}}(n-k+l-1/2)^{\underline{l}}}$$

$$- \frac{1}{2^{k+l}} \sum_{\substack{p=0 \\ l\neq 0}}^{l-1} \frac{(2(n-2k+l-p))^{\underline{2(l-p)}}}{(2(l-p))^{\underline{2(l-p)}}} c_{n,k-l+p,p} \quad (7)$$

and

$$\gamma_{nkl}(r,R) = \left(\frac{R}{r}\right)^{n-2k+2l}\left(1 - \frac{R^2}{r^2}\right)^{k-l-1/2}. \quad (8)$$

In practice, the 2D image formed by the particle's impact positions on the detector is usually captured by a digital camera. As a result, the measured 2D distribution S_m corresponds to the discretized version of the original continuous distribution $S(R, \alpha)$ that can be represented by a matrix of $N_R \times N_\alpha$ regularly shaped pixels, where N_R and N_α are the numbers of radial and angular elements, respectively. The number of particles $(S_m)_{ij}$ captured by a given pixel located at the discrete coordinate (R_i, α_j) is obtained by integrating the continuous distribution $S(R, \alpha)$ over the pixel area and applying the inverse square law to account for the geometric dilution of the particle's density over distance,

$$(S_m)_{ij} \propto \frac{1}{r^2} \int_{\check{R}_i}^{\hat{R}_i} \int_{\check{\alpha}_j}^{\hat{\alpha}_j} S(R, \alpha)R \, dR \, d\alpha, \quad (9)$$

where $\hat{R}_i(\check{R}_i) = R_i + (-)\Delta R/2$, $\hat{\alpha}_j(\check{\alpha}_j) = \alpha_j + (-)\Delta\alpha/2$, and $(\Delta R, \Delta\alpha)$ are the radial and angular pixel width, respectively. By replacing the continuous integral of the unknown function $F(r)\beta_n(r)$ in Eq. (5) with the corresponding Riemann sum and after rearranging the order of the sums, Eq. (9) gives

$$(S_m)_{ij} = \sum_{n=0}^{2N} \sum_{k=0}^{\lfloor n/2 \rfloor} \left[\sum_{i'\geq i}^{N_R} F(r_{i'})\beta_n(r_{i'}) \sum_{l=0}^{\max\{k-1,0\}} \right.$$
$$\left. \times C_{nkl}\Gamma_{nkl}(r_{i'}, R_i)\Delta r \Delta\alpha \right] P_{n-2k}(\cos\alpha_j) \quad (10)$$

with

$$\Gamma_{nkl}(r_{i'}, R_i) = \frac{1}{r_{i'}^2} \int_{\check{R}_i}^{\hat{R}_i} \gamma_{nkl}(r_{i'}, R)R \, dR$$

$$= \left[\frac{1}{2+2l-2k+n}\left(\frac{R}{r_{i'}}\right)^{2+2l-2k+n} \right.$$

$$\left. \times \, {}_2F_1\left(\begin{matrix} 1/2+l-k, 1+l-k+\frac{n}{2} \\ 2+l-k+\frac{n}{2} \end{matrix}; \frac{R^2}{r_{i'}^2}\right) \right]_{\check{R}_i}^{\hat{R}_i}. \quad (11)$$

We note that the definite integral over the angular coordinate α can be replaced by the corresponding Riemann sum with negligible loss in accuracy, providing that the angular pixel size $\Delta\alpha$ is sufficiently small ($\sim 1°$). On the contrary, because the polynomial $\gamma_{nkl}(r, R)$ has a singularity at the position $r = R$ for $k = l$, the integral over the radial coordinates R is evaluated analytically to prevent any significant approximation error.

For the sake of clarity, Eq. (10) can be rewritten more concisely in matrix form,

$$\mathbf{S_m} = \sum_{n=0}^{2N} \sum_{k=0}^{\lfloor n/2 \rfloor} \mathbf{M_{n,n-2k}}\mathbf{F_n} \otimes \mathbf{P_{n-2k}}, \quad (12)$$

where the column vectors $\mathbf{F_n}$ and $\mathbf{P_{n-2k}}$ represent the unknown distribution $F(r_{i'})\beta_n(r_{i'})$ and the Legendre polynomial $P_{n-2k}(\cos\alpha_j)$, respectively, and $\mathbf{M_{n,n-2k}}$ is an upper triangular transformation matrix defined as

$$(M_{n,n-2k})_{ii'} = \sum_{l=0}^{\max\{k-1,0\}} C_{nkl}\Gamma_{nkl}(r_{i'}, R_i)\Delta r \Delta\alpha. \quad (13)$$

As an illustrative example, the analytic form of a few transformation matrix elements (for $n = 0$–4) is listed in Table I.

Finally, by rearranging the sums in Eq. (12), it follows that the measured 2D image formed on the detector can be

TABLE I. Analytic form of the transformation matrix element $(M_{n,n-2k})_{ii'}$ for $n = 0$–4. For the sake of clarity, we have set $\hat{R}_i = R_i + \Delta R/2$ and $\check{R}_i = R_i - \Delta R/2$.

n = 0	$(M_{00})_{ii'} = \dfrac{2\Delta r \Delta\alpha}{r_{i'}}\left[\sqrt{r_{i'}^2 - \check{R}_i^2} - \sqrt{r_{i'}^2 - \hat{R}_i^2}\right]$
n = 1	$(M_{11})_{ii'} = \dfrac{\Delta r \Delta\alpha}{r_{i'}^2}\left[\check{R}_i\sqrt{r_{i'}^2 - \check{R}_i^2} - \hat{R}_i\sqrt{r_{i'}^2 - \hat{R}_i^2} + r_{i'}^2\arcsin\left(\dfrac{\hat{R}_i}{r_{i'}}\right) - r_{i'}^2\arcsin\left(\dfrac{\check{R}_i}{r_{i'}}\right)\right]$
n = 2	$(M_{22})_{ii'} = \dfrac{2\Delta r \Delta\alpha}{3r_{i'}^3}\left[\sqrt{r_{i'}^2 - \check{R}_i^2}\left(2r_{i'}^2 + \check{R}_i^2\right) - \sqrt{r_{i'}^2 - \hat{R}_i^2}\left(2r_{i'}^2 + \hat{R}_i^2\right)\right]$
	$(M_{20})_{ii'} = \dfrac{\Delta r \Delta\alpha}{3r_{i'}^3}\left[\left(r_{i'}^2 - \hat{R}_i^2\right)^{3/2} - \left(r_{i'}^2 + \check{R}_i^2\right)^{3/2}\right]$
n = 3	$(M_{33})_{ii'} = \dfrac{\Delta r \Delta\alpha}{4r_{i'}^4}\left[\check{R}_i\sqrt{r_{i'}^2 - \check{R}_i^2}\left(3r_{i'}^2 + 2\check{R}_i^2\right) - \hat{R}_i\sqrt{r_{i'}^2 - \hat{R}_i^2}\left(3r_{i'}^2 + 2\hat{R}_i^2\right) + 3r_{i'}^4\arcsin\left(\dfrac{\hat{R}_i}{r_{i'}}\right) - 3r_{i'}^4\arcsin\left(\dfrac{\check{R}_i}{r_{i'}}\right)\right]$
	$(M_{31})_{ii'} = \dfrac{3\Delta r \Delta\alpha}{8r_{i'}^4}\left[\check{R}_i\sqrt{r_{i'}^2 - \check{R}_i^2}\left(-r_{i'}^2 + 2\check{R}_i^2\right) - \hat{R}_i\sqrt{r_{i'}^2 - \hat{R}_i^2}\left(-r_{i'}^2 + 2\hat{R}_i^2\right) + r_{i'}^4\arcsin\left(\dfrac{\check{R}_i}{r_{i'}}\right) - r_{i'}^4\arcsin\left(\dfrac{\hat{R}_i}{r_{i'}}\right)\right]$
n = 4	$(M_{44})_{ii'} = \dfrac{2\Delta r \Delta\alpha}{15r_{i'}^5}\left[\sqrt{r_{i'}^2 - \check{R}_i^2}\left(8r_{i'}^4 + 4r_{i'}^2\check{R}_i^2 + 3\check{R}_i^4\right) - \sqrt{r_{i'}^2 - \hat{R}_i^2}\left(8r_{i'}^4 + 4r_{i'}^2\hat{R}_i^2 + 3\hat{R}_i^4\right)\right]$
	$(M_{42})_{ii'} = \dfrac{\Delta r \Delta\alpha}{3r_{i'}^5}\left[\left(r_{i'}^2 - \hat{R}_i^2\right)^{3/2}\left(2r_{i'}^2 + 3\hat{R}_i^2\right) - \left(r_{i'}^2 - \check{R}_i^2\right)^{3/2}\left(2r_{i'}^2 + 3\check{R}_i^2\right)\right]$
	$(M_{40})_{ii'} = \dfrac{\Delta r \Delta\alpha}{60r_{i'}^5}\left[\left(r_{i'}^2 - \hat{R}_i^2\right)^{3/2}\left(21\hat{R}_i^2 - r_{i'}^2\right) - \left(r_{i'}^2 - \check{R}_i^2\right)^{3/2}\left(21\check{R}_i^2 - r_{i'}^2\right)\right]$

expressed as a sum of Legendre polynomials $P_n(\cos\alpha)$

$$\mathbf{S_m} = \sum_{n=0}^{2N} \boldsymbol{\delta_n} \otimes \mathbf{P_n}, \tag{14}$$

whose expansion coefficients $\delta_n(R_i)$ are given by

$$\boldsymbol{\delta_n} = \sum_{k=0}^{N-\lceil n/2 \rceil} \mathbf{M_{n+2k,n}F_{n+2k}}. \tag{15}$$

B. The original 3D distribution reconstruction

To reconstruct the original 3D distribution, both the radial and asymmetry parameter distributions, $F(R)$ and $\beta_n(R)$, respectively, need to be retrieved. Equation (15) shows that the product of these two distributions ($F(R)\beta_n(R)$) can be directly deduced from the coefficients $\delta_n(R)$, which can be determined beforehand by expanding the measured 2D image in a sum of Legendre polynomials. Knowing that $\beta_0(R) = 1$, the radial distribution $F(r)$ is directly obtained from the product $F(R)\beta_0(R)$, allowing, in turn, the determination of the asymmetry parameter distributions $\beta_n(R)$ from the product functions $F(R)\beta_n(R)$. The complete inversion procedure is represented in Fig. 2 and discussed in details below.

1. Cartesian to polar coordinate transformation

The measured 2D raw image, which is generally represented by a matrix of $N_x \times N_z$ pixels in a Cartesian coordinate system, where N_x and N_z are the number of pixels along the x and z axis, respectively, is first converted to a 2D density plot as a function of both polar coordinates (R, α). Because the image exhibits a mirror symmetry along the z direction, the polar coordinate α can run from 0 to either π or 2π depending on whether the two independent measurements ($x > 0$ and $x < 0$) of the 3D distribution are analyzed separately or not. The number of radial (N_R) and angular (N_α) pixels are typically chosen equal to $N_x/2$ (or $N_z/2$) and 360 (or 180), respectively. The pixel intensity at a given position (R_i, α_j) associated with the Cartesian coordinates (x, z) is deduced from the original image by performing a bilinear interpolation between the intensities measured at the four pixels surrounding this particular (x, z) coordinate.

2. Legendre polynomial expansion of the angular component

In the second step, the angular distribution $I_{R_i}(\alpha_j)$ for a given radial position R_i is expanded into a sum of Legendre polynomials $P_k(\cos\alpha)$. By using the orthogonality properties of these polynomials, the expansion coefficients $\delta_k(R_i)$ are obtained from

$$\delta_k(R_i) = \frac{2k+1}{2} \sum_{j=1}^{N_\alpha} |\sin\alpha_j| P_k(\cos\alpha_j) I_{R_i}(\alpha_j)\Delta\alpha, \tag{16}$$

where $\alpha_j = 2\pi j/N_\alpha$ and $\Delta\alpha$ is the angular pixel width.

3. Radial and asymmetry parameter distributions' retrieval

Finally, the distributions $F(R_i)$ and $\beta_k(R_i)$ are directly determined from the expansion coefficients $\delta_k(R_i)$. By
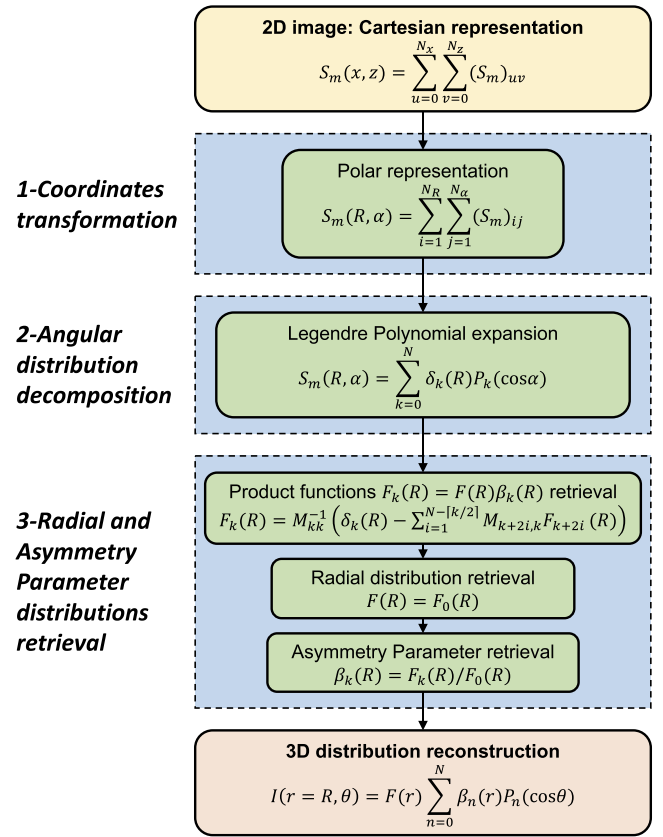

FIG. 2. Flow chart representing the original 3D distribution reconstruction procedure. The procedure consists of three steps: (1) the Cartesian to polar coordinate transformation of the measured 2D raw image, (2) the expansion of the angular distribution in a sum of Legendre polynomials, and (3) the radial and asymmetry parameter distributions retrieval.

recognizing that Eq. (15) is equivalent to two triangular systems of linear equations associated with either even or odd values of k,

$$
\begin{aligned}
\boldsymbol{\delta_{2N}} &= \mathbf{M_{2N,2N}F_{2N}} \\
&\vdots \\
\boldsymbol{\delta_2} &= \mathbf{M_{2N,2}F_{2N}} + \cdots + \mathbf{M_{42}F_4} + \mathbf{M_{22}F_2} \\
\boldsymbol{\delta_0} &= \mathbf{M_{2N,0}F_{2N}} + \cdots + \mathbf{M_{40}F_4} + \mathbf{M_{20}F_2} + \mathbf{M_{00}F_0}
\end{aligned} \tag{17}
$$

and

$$
\begin{aligned}
\boldsymbol{\delta_{2N-1}} &= \mathbf{M_{2N-1,2N-1}F_{2N-1}} \\
&\vdots \\
\boldsymbol{\delta_3} &= \mathbf{M_{2N-1,3}F_{2N-1}} + \cdots + \mathbf{M_{33}F_3} \\
\boldsymbol{\delta_1} &= \mathbf{M_{2N-1,1}F_{2N-1}} + \cdots + \mathbf{M_{31}F_3} + \mathbf{M_{11}F_1},
\end{aligned} \tag{18}
$$

respectively, the product functions $\mathbf{F_k}$ can be determined recursively by using the method of back-substitution,

$$\mathbf{F_k} = \mathbf{M_{kk}^{-1}}\left(\delta_k - \sum_{i=1}^{2N-\lceil k/2 \rceil} \mathbf{M_{k+2i,k}F_{k+2i}}\right). \tag{19}$$

Knowing that $\beta_0(R_i) = 1$, the radial and asymmetry parameter distributions are finally deduced from Eq. (19),

$$F(R_i) = F_0(R_i),$$
$$\beta_k(R_i) = \frac{F_k(R_i)}{F_0(R_i)}. \tag{20}$$

III. RESULTS

A. Inversion of model images

The performance of the algorithm was first tested on model images generated from simulated experiments. A conventional Monte Carlo procedure was used to mimic a three-dimensional particle emission defined by a given distribution $I(r, \theta, \varphi)$. The spherical coordinates (r, θ) were independently selected according to the chosen radial (velocity) $F(r)\beta_n(r)$ and angular $P_n(\cos\theta)$ distributions, while the azimuthal angle φ was uniformly distributed. The simulated events were then binned into a 1024×1024 two-dimensional array based on their Cartesian coordinates $x = r\sin\theta\cos\varphi$ and $z = r\cos\theta$ to form the model image. The number of simulated events was chosen between 10^4 and 10^9 depending on the desired image quality.

1. One-photon ionization experiment

We first apply the reconstruction procedure on model images resulting from a single-photon ionization experiment with linearly polarized light. In such an experiment, the particle's angular distribution can be expanded as a sum of the Legendre polynomials P_0 and P_2,[32,33]

$$I(r, \theta) = F(r)\left[1 + \beta_2(r)P_2(\cos\theta)\right]. \tag{21}$$

According to Eqs. (14) and (15), the measured 2D image can also be expressed as a sum of two even-order Legendre polynomials,

$$S_m(R_i, \alpha_j) = \delta_0(R_i)P_0(\cos\alpha_j) + \delta_2(R_i)P_2(\cos\alpha_j), \tag{22}$$

where

$$\delta_0(R_i) = M_{00}F(R_i) + M_{20}F(R_i)\beta_2(R_i),$$
$$\delta_2(R_i) = M_{22}F(R_i)\beta_2(R_i). \tag{23}$$

Using Eqs. (19) and (20), the distributions $F(R_i)$ and $\beta_2(R_i)$ can then be directly retrieved from the measured coefficients $\delta_0(R_i)$ and $\delta_2(R_i)$,

$$F(R_i) = M_{00}^{-1}\left[\delta_0(R_i) - M_{20}M_{22}^{-1}\delta_2(R_i)\right],$$
$$\beta_2(R_i) = \frac{M_{22}^{-1}\delta_2(R_i)}{M_{00}^{-1}\left[\delta_0(R_i) - M_{20}M_{22}^{-1}\delta_2(R_i)\right]}. \tag{24}$$

To evaluate the performance of our method, 3D emissions having distinct radial (velocity) distributions and constant asymmetry parameters $[\beta_2(R) = 1]$ are first considered. The radial distributions are composed of a series of Gaussian peaks having various intensities [Fig. 3(c)] or widths [Fig. 4(c)] as reported in Table II. Model images shown in Figs. 3(a) and 4(a) were first generated by accumulating 10^9 events and then converted to polar density plots (not shown). Subsequently, the angular distributions at each radial position R_i were expanded as a sum of Legendre polynomials. Using
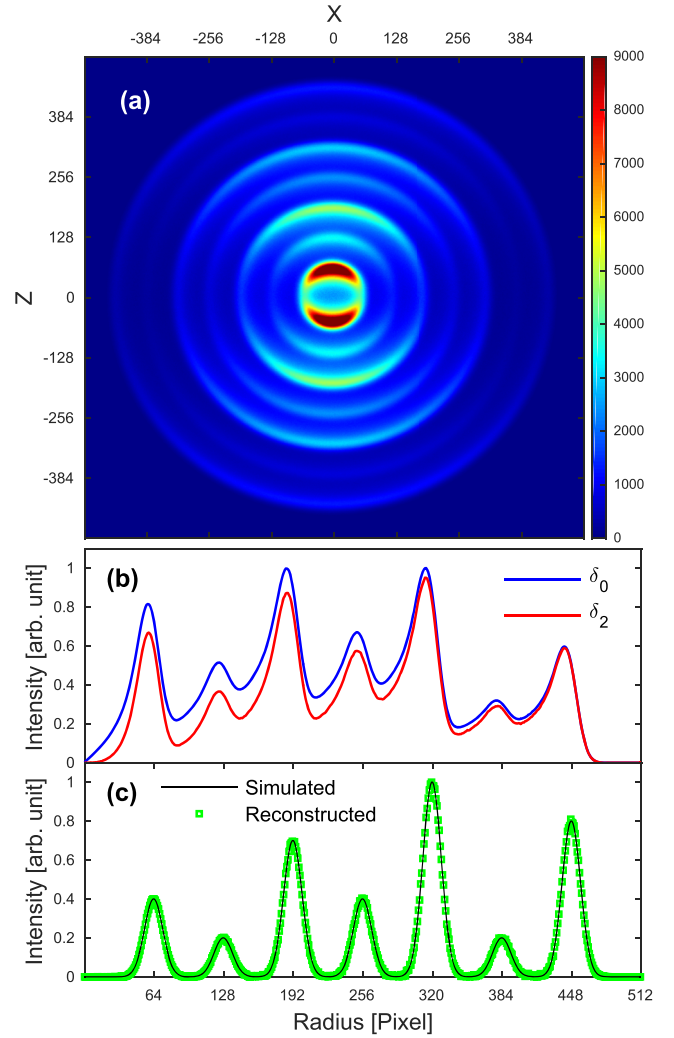

FIG. 3. Experiment 1: (a) Simulated image for a linearly polarized one-photon ionization experiment (10^9 events). The radial distribution of the emerging particles is modeled as a series of Gaussian peaks, with each having the same width and distinct intensities. (b) Legendre polynomial expansion coefficients of the simulated image. (c) Reconstructed (green square) and simulated (black line) radial distributions.

Eqs. (24), the radial distributions were finally reconstructed from the resulting expansion coefficients plotted in Figs. 3(b) and 4(b). As can be seen in Figs. 3(c) and 4(c), there is an excellent agreement between the reconstructed and simulated distributions. The width, shape, and intensity of each peak are retrieved almost perfectly, even in the case where the width of

TABLE II. Properties (radial distribution) of the one-photon simulations shown in Figs. 3 and 4.

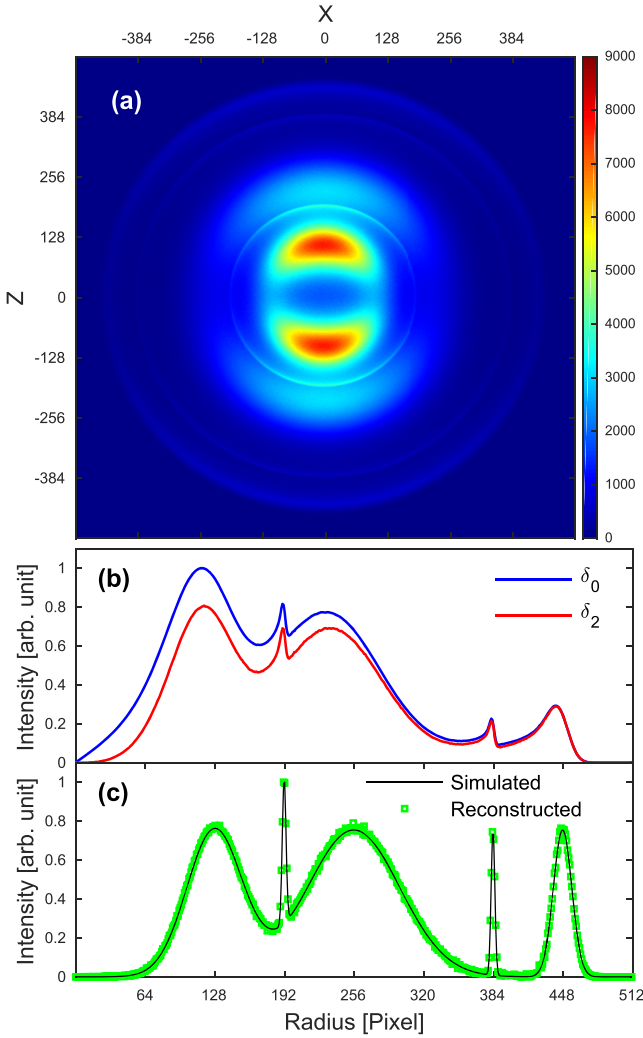| Peak	Experiment 1 (Fig. 3)			Experiment 2 (Fig. 4)		
	Center	FWHM	Intensity	Center	FWHM	Intensity
1	64	20	0.4	128	60	1
2	128	20	0.2	192	4	1
3	192	20	0.7	256	100	1
4	256	20	0.4	384	4	1
5	320	20	1.0	448	20	1
6	384	20	0.2			
7	448	20	0.8			

FIG. 4. Experiment 2: (a) Simulated image for a linearly polarized one-photon ionization experiment (10^9 events). The radial distribution of the emerging particles is modeled as a series of Gaussian peaks, with each having the same intensity and distinct widths. (b) Legendre polynomial expansion coefficients of the simulated image. (c) Reconstructed (green square) and simulated (black line) radial distributions.
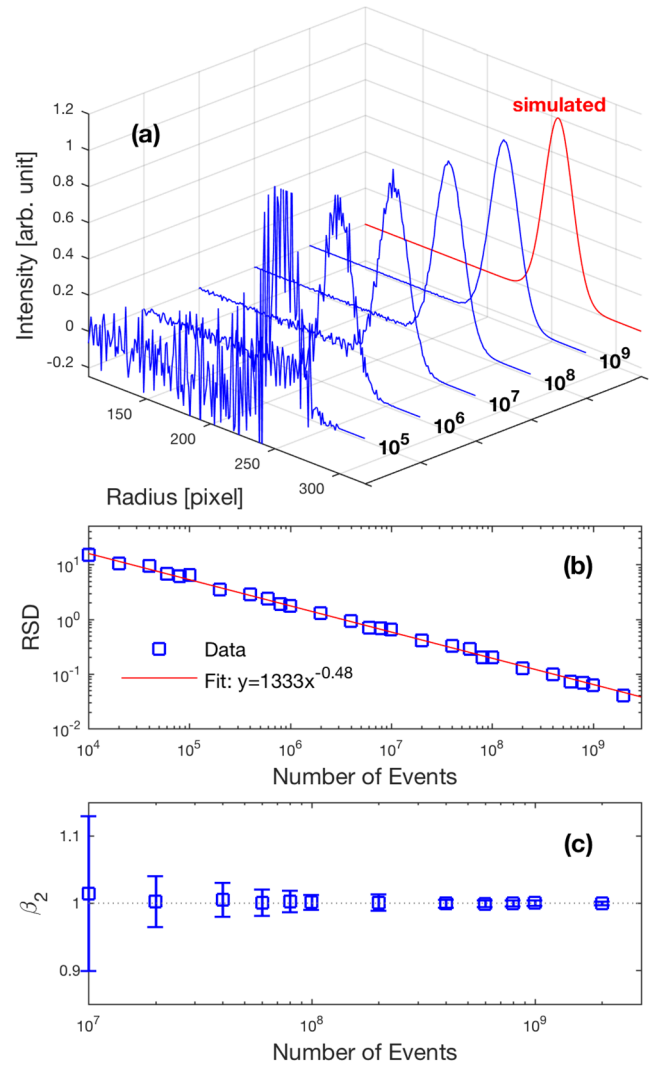

FIG. 5. Effect of the image quality (represented by the number of simulated events) on the goodness of the reconstruction: (a) reconstructed radial distribution, (b) relative standard deviation (RSD) of the radial distribution (square), and (c) asymmetry parameter β.

the peak becomes comparable to the pixel width, as shown in Fig. 4(c) (see peaks #2 and #4). In addition, the level of noise in the region of the reconstructed spectrum where the signal is low (in-between the peaks) is unnoticeable. These observations show that the performance of the reconstruction does not depend on the peak intensity or width providing that the image quality is high enough.

To estimate the effect of the image quality on the goodness of the reconstruction, we then vary the number of simulated events accumulated in the model images. For simplicity, we consider here a radial distribution made of a single Gaussian peak located at the center of the distribution ($R = 256$ pixels) and having a FWHM equal to 5% of the full distribution range (25.6 pixels). The reconstructed radial distribution as a function of the number of accumulated events is plotted in Fig. 5(a). As expected, the quality of the reconstructed distribution increased with the number of events. For a low number of accumulated events (10^5), the level of noise is quite high compared to the original signal, making it difficult to

recognize the presence of a single Gaussian peak in the distribution (small lobes might be observed on each sides of the peak). As the number of events increases, the level of noise decreases rapidly. For a sufficiently high number of events (10^9), the reconstructed and simulated distributions become almost indistinguishable. To assess whether the deviation between the reconstructed and simulated distributions is due to statistical noise and not due to systematic departures from the original distribution, we have evaluated the relative standard deviation (RSD) of the reconstructed distribution according to

$$\text{RSD} = \sqrt{\frac{1}{N_R} \sum_{i=1}^{N_R} \left[(y_r)_i - (y_s)_i \right]^2} \bigg/ \overline{y_s}, \qquad (25)$$

where y_r and y_s represent the intensities of the reconstructed and simulated distributions, respectively, and $\overline{y_s} = \pi \text{FWHM}/2\sqrt{\ln 2} N_R$ is the average value of the Gaussian distribution over the full spectrum range ($N_R = 512$). The relative standard deviation as a function of the number of events is shown in Fig. 5(b). We can see that the relative standard

deviation decreases nearly inversely with the square root of the number of events, which indicates that the deviation between the reconstructed and simulated distributions is governed by Poisson statistics. From this observation, we can conclude that the quality of the reconstructed spectrum is mainly determined by the statistical noise, while the goodness of the reconstruction is independent of the image quality. Perhaps more surprising is that the statistical noise distribution accumulates preferentially toward the low R values. The origin of this effect lies in the relationship between the radial distribution and the measured coefficients δ_k. As shown in Eq. (19), where the matrices M_{kk}^{-1} are triangular, the fraction of the measured distribution δ_k used in the reconstruction of the radial distribution increases as R decreases. As a consequence, the statistical noise adds up increasingly in the reconstructed distribution toward the low R values. A similar effect has been observed with other methods,[22,24] which have reported an accumulation of the noise toward the image center, and is inherent to any 2D-to-3D inversion procedure in one way or another.

Finally, the dependence of the goodness of the reconstruction on the image quality is further illustrated in Fig. 5(c), where we have plotted the retrieved value of the asymmetry parameter β_2 as a function of the number of accumulated events (the parameter has been averaged over the peak width, and the standard deviation from the mean value gives an estimated error in the reconstruction). It can be seen that the retrieved asymmetry parameter matches the simulated value ($\beta_2 = 1$) rather well for any number of accumulated events. In addition, we have found that the deviation between the retrieved and simulated values is due to statistical noise and not due to a systematic error resulting from the reconstruction. These findings confirm our previous conclusion that the performance of the reconstruction is independent of the image quality.

2. Multi-photon ionization process

To further evaluate the ability of our procedure to accurately retrieve asymmetry parameters, we now turn our attention to the case of a two-color two-photon experiment, where the particle's angular distribution can be expanded as a sum of both odd- and even-order Legendre polynomials.[39–41] The properties of the particle emission considered here are given in Table III. The asymmetry parameters β_n were set to different values, while the radial distribution

is made of a series of Gaussian peaks with constant intensities and widths. As before, a model image was first generated by accumulating 10^9 events and then converted to a polar density plot. According to Eqs. (14) and (15), the measured 2D image was then expanded as a sum of five Legendre polynomials,

$$S_m(R_i, \alpha_j) = \sum_{k=0}^{4} \delta_k(R_i) P_n(\cos \alpha_j), \quad (26)$$

and both the radial distribution and the asymmetry parameters were subsequently deduced from the resulting expansion coefficients δ_k, using Eqs. (19) and (20). We note that compared to the case of one-photon experiments, the radial distribution is now reconstructed from three expansion coefficients (δ_0, δ_2, and δ_4). In addition, the even-order asymmetry parameters (β_2 and β_4) are retrieved from even-order expansion coefficients only, while the odd-order asymmetry parameters (β_1 and β_3) are deduced from both odd- and even-order coefficients.

The reconstructed radial distribution and retrieved asymmetry parameters (averaged over the peak width) are shown in Fig. 6. Again, it can be seen that there is an excellent agreement between the reconstructed and simulated distributions. Both the intensity and width of the radial distribution are reconstructed accurately, while the retrieved asymmetry parameters are within only a few percent of the simulated values. It is interesting to observe that the parameter β_1 is retrieved more accurately than any other parameter, as shown by their margins of error. Due to statistical error propagation, one would think that the uncertainty increases with the number of coefficients δ_k used in the reconstruction. However, Fig. 6(c) suggests that the margins of error decrease with the order of the asymmetry parameters indicating that this is not the case. We do not yet have an explanation for this effect, but we have observed that the level of statistical noise in the distribution $F(R)\beta_k(R)$ decreases with the order k. This implies that an effect of self-compensation for the statistical error may occur. Further investigation of this question would be a separate, and very worthy, endeavor.

3. DAVIS vs pBASEX

We now compare the level of performance of our method and the pBASEX technique[24] for inverting model images. To that purpose, one-photon absorption induced emissions having distinct radial (velocity) distributions and non-constant asymmetry parameters are considered. The radial distributions are composed of a series of peaks having either Gaussian or Lorentzian shapes with the properties reported in Table IV. Model images were first generated by accumulating 10^9 events and then inverted using both methods. The number and width of Gaussian basis functions used in the pBASEX inversion were set equal to 256 and $\sqrt{2}$, respectively, while the number of Legendre polynomials was defined by the physics of the photoionization process.

As can be seen in Fig. 7, both methods lead to almost identical reconstructed distributions and asymmetry parameters. The width, shape, and intensity of each peak match perfectly, even in the case where the peak intensity is low (see peaks #2

TABLE III. Properties (radial distribution and β-parameter) of the two-photon simulation shown in Fig. 6.

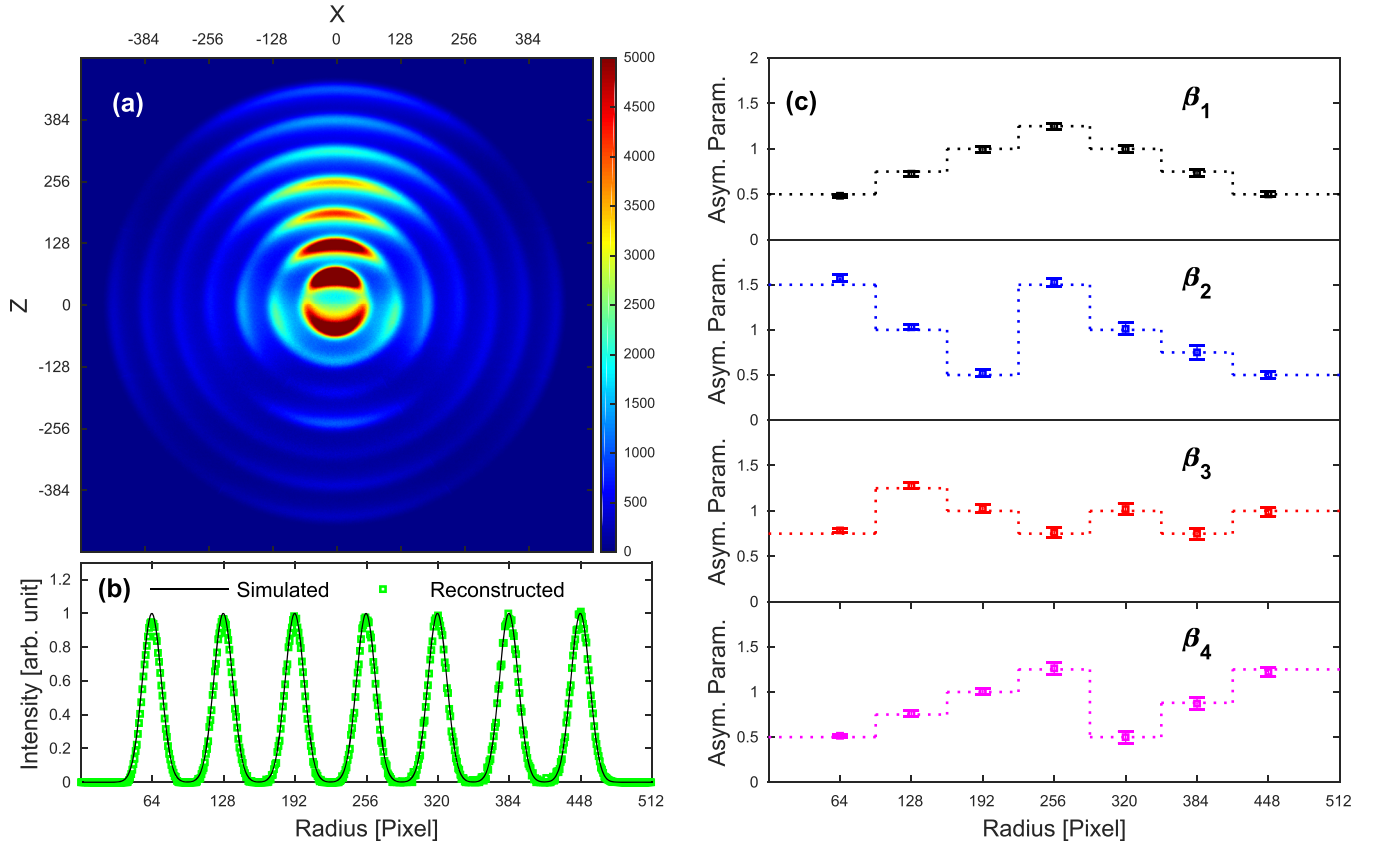| Peak	Center	FWHM	Intensity	β_1	β_2	β_3	β_4
1	64	20	1	0.5	1.5	0.75	0.5
2	128	20	1	0.75	1	1.25	0.75
3	192	20	1	1	0.5	1	1
4	256	20	1	1.25	1.5	0.75	1.25
5	320	20	1	1	1	1	0.5
6	384	20	1	0.75	0.75	0.75	0.88
7	448	20	1	0.5	0.5	1	1.25

FIG. 6. Case of a two-color two-photon experiment: (a) simulated image (10^9 events), (b) reconstructed (green square) and simulated (black line) radial distributions, and (c) retrieved (square) and simulated (dotted line) asymmetry parameters β_n.

and #4). This shows that both methods offer a similar level of performance in terms of accuracy in the absence of any noise or background, providing that the number of Gaussian basis functions used in pBASEX is large enough to reproduce the features of the 3D distribution.[42]

B. Inversion of experimental data

To test the robustness of the procedure in the presence of experimental noise and background, our algorithm has been applied to experimental images formed by collecting the photoelectrons generated from one-photon ionization of argon atoms with an attosecond pulse train. The experiment was performed with a setup that combines a Ti:sapphire laser delivering 35-fs 800-nm pulses, an attosecond pulse source, and a

TABLE IV. Properties (radial distribution and β-parameter) of the one-photon simulation shown in Fig. 7.

| Peak | Center | FWHM | | Intensity | β_2 |
		Gaussian	Lorentzian		
1	80	20	5	0.8	1.5
2	130	15	3.75	0.1	1
3	240	80	20	1	0.5
4	330	15	3.75	0.1	1.5
5	400	60	15	0.6	1

home-made velocity-map imaging system.[44] Attosecond pulse trains made of odd harmonics of the fundamental 800-nm field were generated in argon via high harmonic generation. The pulse trains were then filtered to remove harmonics below the 11th order and finally focused into an ultra-high vacuum chamber where the velocity-map imaging system was located. Images were captured with a CMOS camera (1000×1000 pixels) that recorded the photoelectron's impact positions on a MCP/phosphor position sensitive detector.

A typical image is shown in Fig. 8(a). This image was formed by collecting photoelectrons produced by roughly 10^6 pulse trains, and its center was determined using a procedure reported recently.[45] Each ring observed in the image corresponds to the photoionization of the $3p$ electrons of argon by a given odd harmonic (11th–21th). Their width is directly related to the attosecond pulse train duration, which has been estimated around 15 fs. On the other hand, the ghost features appearing in the image in the form of inclined parallel lines are attributed to photoelectrons generated from the residual gas (mainly argon) along the direction of propagation of the pulse trains inside the velocity-map imaging spectrometer.

The radial distributions reconstructed with both our algorithm (DAVIS) and the pBASEX technique[24] are shown in Fig. 8(b). Overall, the reconstructed distributions are quite similar. Both methods retrieve the main components of the distribution and lead to comparable results for both the position and the width of each peak. The most notable difference
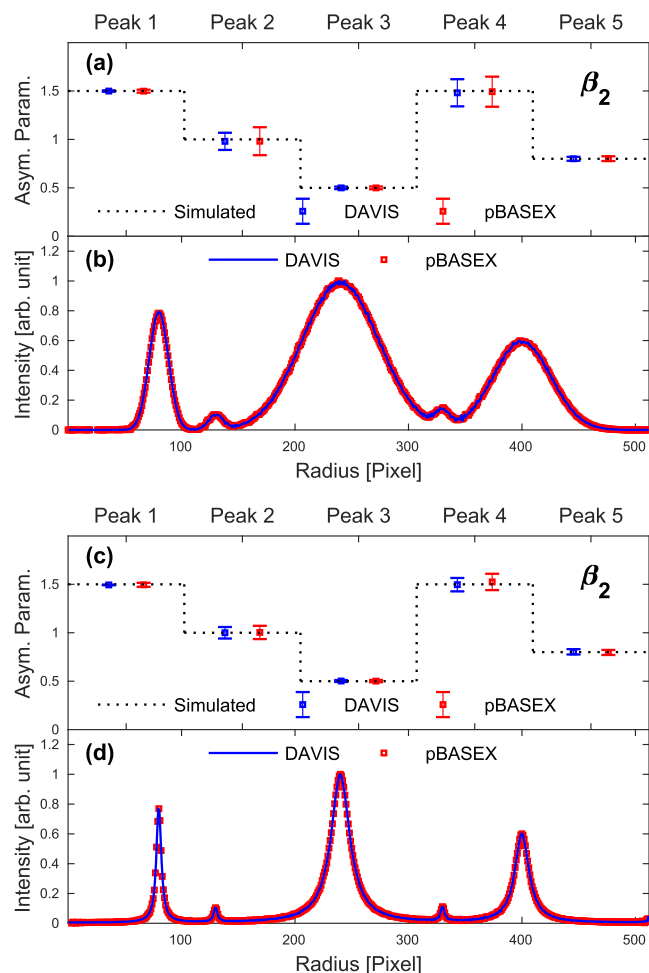
FIG. 7. Asymmetry parameters [(a) and (c)] and radial distributions [(b) and (d)] reconstructed with DAVIS and pBASEX from model images resulting from one-photon induced emissions having either a Gaussian [(a) and (b)] or Lorentzian [(c) and (d)] radial distribution. Images were generated by accumulating 10^9 events.
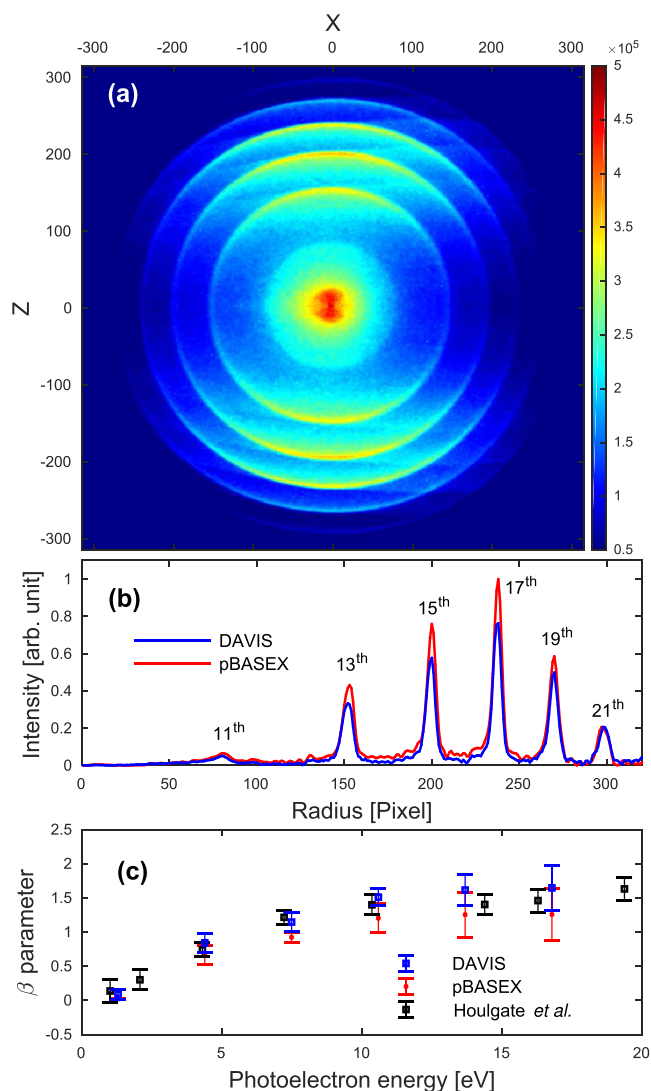

FIG. 8. (a) Experimental image obtained for the one-photon ionization of argon by a linearly polarized attosecond pulse train made of odd harmonics, (b) reconstructed radial distributions obtained with DAVIS and pBASEX,[24] and (c) asymmetry parameters retrieved with DAVIS (blue square) and pBASEX (red point), and previously measured by Houlgate *et al.*[43] (black square).

observed between these distributions is the peak intensities. The intensities retrieved with DAVIS are somewhat lower than those obtained with pBASEX. Such a difference is directly related to the image noise and/or background propagating into the reconstructed radial distributions. With DAVIS, most of the image noise and background is first filtered out from the meaningful angle-correlated signal by the Legendre polynomial expansion before inversion. On the other hand, pBASEX does not prefilter the measured image before inversion. As a result, the image noise (background), like the ghost lines observed in Fig. 8(a), eventually contributes to the peak intensity, as can be seen in Fig. 8(b).

Finally, the robustness of our method in the presence of noise (background) is further demonstrated in the measurement of the asymmetry parameters β. The retrieved parameters obtained with both DAVIS and pBASEX are shown in Fig. 8(c). The parameters have been averaged over the peak width, and the standard deviation from the mean value gives an estimated error in their measurement. The results of a previous study,[43] where the β parameters were obtained by direct measurement of the angular distribution using a rotatable electron analyzer, are also plotted. Overall, there is good agreement

between the β parameters retrieved with both DAVIS and pBASEX and those measured by Houlgate *et al.* However, we can see that the parameters retrieved with pBASEX are consistently lower than those obtained with DAVIS. This results from the fact that the image noise and background do not contribute equally to the reconstructed radial distribution associated with each Legendre polynomial (i.e., P_0 and P_2). In fact, we have observed in the reconstruction with pBASEX that the noise (background) contributes more to the radial distribution associated with P_0, which consequently leads to lower values for the asymmetry parameters.

C. Retrieval time

To conclude this study, it is worth devoting a few words to the computation time needed to reconstruct the 3D distributions from the 2D images. Our algorithm has been implemented in LABVIEW 2017 on a computer equipped with a
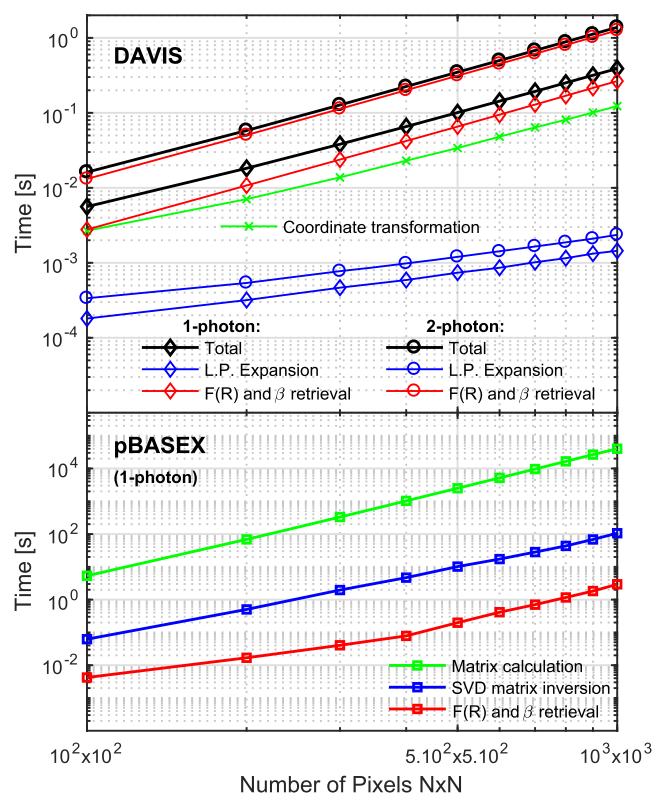
FIG. 9. Reconstruction times as a function of the image resolution (number of pixels $N_x \times N_z$) for the case of a one-photon (diamond) and a two-photon (circle) experiment: computation time for the coordinates transformation (green), the Legendre polynomial expansion (blue), and the radial and β parameter distributions retrieval (red), as well as the total reconstruction time (black). As a comparison, the characteristic times of the pBASEX inversion[24] for the case of a one-photon experiment are also shown: computation time for the matrix calculation (green), the matrix inversion (blue), and the radial and β parameter distributions retrieval (red).

3.3 GHz Intel Core i5-4590 processor, 8 GB RAM, and a 64-bit Windows operating system. The dependence of the reconstruction time on the image resolution, defined by the number of pixels $N_x \times N_z$, is shown in Fig. 9. It can be readily seen that the method is computationally fast, as it only takes around 0.4 and 1.4 s to invert a 1000×1000 image resulting from a one-photon and a two-photon experiments, respectively. As a comparison, it takes about 3 s for the pBASEX method[24] to invert an image with the same resolution that results from a one-photon experiment [assuming that the time-consuming matrix calculation (~11 h) and inversion (~2 min) have been performed beforehand]. Such a difference in the reconstruction times results from the fact that our procedure uses matrices of lower dimension ($N_R \times N_R$) compared to those embedded in pBASEX ($N_R^2 \times N_k N_l$, where N_k and N_l are the number of radial and angular basis functions used in the reconstruction, respectively).

More specifically, the reconstruction time is dominated by the computation time needed to retrieve both the radial distribution and the asymmetry parameters from the expansion coefficients δ_n. This is because the matrix calculations and the subsequent operations involved in this step of the procedure are relatively slow. We note that the number of matrices involved in the procedure increases with the number of coefficients, which explains the difference between the one-photon and

two-photon reconstruction times. By comparison, the computation time needed to expand the image as a sum of Legendre polynomials is very short (around 1 ms) and only slightly increases with the number of terms in the expansion. On the other hand, the computation time required for transforming the image from a Cartesian to polar representation, which only depends on the total number of pixels $N_R \times N_\alpha$ in the density plot, is on the order of tens of milliseconds. In addition, we have found that the computational speed of our method nearly scales as N^2, which is somewhat faster than other methods.[19,22]

IV. CONCLUSIONS

In this work, we have developed a novel procedure, called DAVIS (Direct Algorithm for Velocity-map Imaging System), to reconstruct the 3D momentum distribution of the charged particles (photoelectrons and photoions) collected with a velocity-map imaging system. The method consists of fitting the measured image with the 2D projection of a model 3D velocity distribution defined by the physics of the light-matter interaction, much like the pBASEX technique does. Both methods show a similar level of performance in terms of accuracy for inverting high quality images with a low level of noise or background. However, our method offers two main advantages over pBASEX. It is computationally faster as the 2D projection function is evaluated analytically rather than numerically and because the procedure involves matrices of lower dimension compared to those embedded in pBASEX. In addition, it is less sensitive to noise and/or background as the meaningful angle-correlated information is extracted from the raw data before inversion by expanding the image with a complete set of Legendre polynomials. Overall, our algorithm is simple, easy to implement, and explicitly takes into account the pixelization effect in the measurement. Due to its high computational speed, it is well-suited for experiments that require fast image-based feedback.

[1]D. W. Chandler and P. L. Houston, J. Chem. Phys. **87**, 1445 (1987).
[2]A. T. J. B. Eppink and D. H. Parker, Rev. Sci. Instrum. **68**, 3477 (1997).
[3]B. J. Whitaker, *Imaging in Molecular Dynamics: Technology and Applications* (Cambridge University Press, Cambridge, 2003).
[4]R. N. Bracewell, *The Fourier Transform and its Applications*, 3rd ed. (McGraw Hill, Boston, 2000).
[5]L. M. Smith, IEEE Trans. Inf. Theory **34**, 158 (1988).
[6]K. Tonokura and T. Suzuki, Chem. Phys. Lett. **224**, 1 (1994).
[7]C. R. Gebhardt, T. P. Rakitzis, P. C. Samartzis, V. Ladopoulos, and T. N. Kitsopoulos, Rev. Sci. Instrum. **72**, 3848 (2001).

[8]J. J. Lin, J. Zhou, W. Shiu, and K. Liu, Rev. Sci. Instrum. **74**, 2495 (2003).

[9]D. Townsend, M. P. Minitti, and A. G. Suits, Rev. Sci. Instrum. **74**, 2530 (2003).

[10]V. Papadakis and T. N. Kitsopoulos, Rev. Sci. Instrum. **77**, 083101 (2006).

[11]J. O. F. Thompson, C. Amarasinghe, C. Foley, and A. G. Suits, J. Chem. Phys. **147**, 013913 (2017).

[12]S. M. Candel, Comput. Phys. Commun. **23**, 343 (1981).

[13]L. M. Smith, D. R. Keefer, and S. I. Sudharsanan, J. Quant. Spectrosc. Radiat. Transfer **39**, 367 (1988).

[14]Y. Sato, Y. Matsumi, M. Kawasaki, K. Tsukiyama, and R. Bersohn, J. Phys. Chem. **99**, 16307 (1995).

[15]C. Bordas, F. Paulig, H. Helm, and D. L. Huestis, Rev. Sci. Instrum. **67**, 2257 (1996).

[16]J. Winterhalter, D. Maier, J. Honerkamp, V. Schyja, and H. Helm, J. Chem. Phys. **110**, 11187 (1999).

[17]K. Zhao, T. Colvin, W. T. Hill III, and G. Zhang, Rev. Sci. Instrum. **73**, 3044 (2002).

[18]S. Manzhos and H.-P. Loock, Comput. Phys. Commun. **154**, 76 (2003).

[19]G. M. Roberts, J. L. Nixon, J. Lecointre, E. Wrede, and J. R. R. Verlet, Rev. Sci. Instrum. **80**, 053104 (2009).

[20]C. E. Rallis, T. G. Burwitz, P. R. Andrews, M. Zohrabi, R. Averin, S. De, B. Bergues, B. Jochim, A. V. Voznyuk, N. Gregerson, B. Gaire, I. Znakovskaya, J. McKenna, K. D. Carnes, M. F. Kling, I. Ben-Itzhak, and E. Wells, Rev. Sci. Instrum. **85**, 113105 (2014).

[21]M. Brouard, S. D. S. Gordon, B. Nichols, E. Squires, V. Walpole, F. J. Aoiz, and S. Stolte, J. Chem. Phys. **146**, 204304 (2017).

[22]M. J. J. Vrakking, Rev. Sci. Instrum. **72**, 4084 (2001).

[23]V. Dribinski, A. Ossadtchi, V. A. Mandelshtam, and H. Reisler, Rev. Sci. Instrum. **73**, 2634 (2002).

[24]G. A. Garcia, L. Nahon, and I. Powis, Rev. Sci. Instrum. **75**, 4989 (2004).

[25]V. K. Nestorov, R. D. Hinchliffe, R. Uberna, J. I. Cline, K. T. Lorenz, and D. W. Chandler, J. Chem. Phys. **115**, 7881 (2001).

[26]M. J. Bass, M. Brouard, A. P. Clark, and C. Vallance, J. Chem. Phys. **117**, 8723 (2002).

[27]S. Manzhos and H.-P. Loock, Rev. Sci. Instrum. **75**, 2435 (2004).

[28]F. Renth, J. Riedel, and F. Temps, Rev. Sci. Instrum. **77**, 033103 (2006).

[29]R. A. Livingstone, J. O. F. Thompson, M. Iljina, R. J. Donaldson, B. J. Sussman, M. J. Paterson, and D. Townsend, J. Chem. Phys. **137**, 184304 (2012).

[30]T. Gerber, Y. Liu, G. Knopp, P. Hemberger, A. Bodi, P. Radi, and Y. Sych, Rev. Sci. Instrum. **84**, 033101 (2013).

[31]B. Dick, Phys. Chem. Chem. Phys. **16**, 570 (2014).

[32]R. N. Zare, *Angular Momentum: Understanding Spatial Aspects in Chemistry and Physics* (Wiley, New York, 1988).

[33]K. Reid, Annu. Rev. Phys. Chem. **54**, 397 (2003).

[34]S. De, M. Magrakvelidze, A. Bocharova, D. Ray, W. Cao, I. Znakovskaya, H. Li, Z. Wang, G. Laurent, U. Thumm, M. F. Kling, I. V. Litvinyuk, I. Ben-Itzhak, and C. L. Cocke, Phys. Rev. A **84**, 043410 (2011).

[35]H. Li, D. Ray, S. De, I. Znakovskaya, W. Cao, G. Laurent, Z. Wang, M. F. Kling, A. T. Le, and C. L. Cocke, Phys. Rev. A **84**, 043429 (2011).

[36]G. Laurent, W. Cao, I. Ben-Itzhak, and C. L. Cocke, in *Multiphoton Processes and Attosecond Physics*, edited by K. Yamanouchi and K. Midorikawa (Springer-Verlag, Berlin Heidelberg, 2012), Chap. 28, pp. 173–177.

[37]G. Laurent, W. Cao, I. Ben-Itzhak, and C. L. Cocke, Opt. Express **21**, 16914 (2013).

[38]G. M. Laurent and G. R. Harrison, "The scaling properties and the multiple derivative of Legendre polynomials," e-print arXiv:math.CA/1711.00925 (2017).

[39]S. J. Smith and G. Leuchs, Adv. At. Mol. Phys. **24**, 157 (1988).

[40]G. Laurent, W. Cao, H. Li, Z. Wang, I. Ben-Itzhak, and C. L. Cocke, Phys. Rev. Lett. **109**, 083001 (2012).

[41]G. Laurent, W. Cao, I. Ben-Itzhak, and C. L. Cocke, J. Phys.: Conf. Ser. **488**, 012008 (2014).

[42]Y. Meyer, *Wavelets and Operators* (Cambridge University Press, Cambridge, 1992).

[43]R. G. Houlgate, J. B. West, K. Codling, and G. V. Marr, J. Electron Spectrosc. Relat. Phenom. **9**, 205 (1976).

[44]N. Kling, D. Paul, A. Gura, G. Laurent, S. De, H. Li, Z. Wang, B. Ahn, C. Kim, T. Kim, I. Litvinyuk, C. Cocke, I. Ben-Itzhak, D. Kim, and M. Kling, J. Instrum. **9**, P05005 (2014).

[45]J. R. Gascooke, S. T. Gibson, and W. D. Lawrance, J. Chem. Phys. **147**, 013924 (2017).